JVST A
Journal of Vacuum Science & Technology A

ARTICLE

avs.scitation.org/journal/jva

Molecular beam epitaxy of polar III-nitride resonant tunneling diodes

Cite as: J. Vac. Sci. Technol. A 39, 023409 (2021); doi: 10.1116/6.0000775
Submitted: 10 November 2020 · Accepted: 11 January 2021 ·
Published Online: 9 February 2021

Jimy Encomendero,[1,a] SM Islam,[1] Debdeep Jena,[1,2,3] and Huili Grace Xing[1,2,3,b]

AFFILIATIONS

[1]School of Electrical and Computer Engineering, Cornell University, Ithaca, New York 14853
[2]Department of Materials Science and Engineering, Cornell University, Ithaca, New York 14853
[3]Kavli Institute at Cornell for Nanoscale Science, Cornell University, Ithaca, New York 14853

Note: This paper is part of the Special Topic Collection: Honoring Dr. Art Gossard's 85th Birthday and his Leadership in the Science and Technology of Molecular Beam Epitaxy.

[a]**Author to whom correspondence should be addressed:** jje64@cornell.edu
[b]**Electronic mail:** grace.xing@cornell.edu

ABSTRACT

Advances in molecular beam epitaxy (MBE) have been crucial for the engineering of heterostructures in which the wave nature of electrons dictates carrier transport dynamics. These advances led to the first demonstration of negative differential conductance (NDC) in arsenide-based resonant tunneling diodes (RTDs) in 1974. In contrast to the 17 years elapsed between the initial MBE growth of arsenide semiconductors and the first demonstration of room-temperature GaAs/AlAs RTDs, the development of polar III-nitride RTDs has been remarkably different. After pioneering growths of nitride materials by MBE in 1973, it would take 43 years—until 2016—to demonstrate the first GaN/AlN RTD that exhibits repeatable NDC at room temperature. Here, we discuss, from the crystal growth point of view, the key developments in the epitaxy of III-nitride heterostructures that have led us to the demonstration of robust resonant tunneling transport and reliable NDC in III-nitride semiconductors. We show that *in situ* tracking of the crystal electron diffraction allows us to deterministically control the number of monolayers incorporated into the tunneling barriers of the active region. Employing this technique, we fabricate various GaN/AlN RTD designs showing the exponential enhancement of the resonant tunneling current as a function of barrier thickness. In addition, we experimentally demonstrate that tunneling transport in nitride RTDs is sensitive to epitaxial parameters such as the substrate growth temperature and threading dislocation density. This new insight into the MBE growth of nitride resonant tunneling devices represents a significant step forward in the engineering of new functionalities within the family of III-nitride semiconductors, allowing to harness quantum interference effects for the new generation of electronic and photonic devices.

I. INTRODUCTION

A cornerstone in the theory of quantum mechanics is the description of particles such as electrons in terms of their wave function. This revolutionary idea[1,2] had far-reaching implications, such as the possibility of electronic matter waves to tunnel across potential barriers. Experimental evidence of this phenomenon was quickly found in 1928 by Oppenheimer,[3] Fowler and Nordheim,[4] and Gamow.[5] A few decades after the initial discovery of this quantum phenomenon, Zener and Esaki pointed out that electronic transport within crystalline materials, such as dielectrics[6] and semiconductors,[7] can also occur via electron tunneling. These important discoveries and the increasingly high interest in semiconductor materials led to the initiative of artificially engineering the electronic tunneling processes within semiconductor heterostructures.

One way to enhance the electronic transmission probability is by using a resonant tunneling cavity, thereby promoting constructive quantum interference of the electronic wave function. This idea was initially proposed to be implemented in dielectric-metallic-dielectric junctions.[8,9] However, the engineering of resonant tunneling structures requires precise control over the thickness of the tunneling barriers and width of the quantum well, on the order of the electron wavelength. Therefore, the first demonstration of resonant tunneling

transport had to await the development of the first molecular beam epitaxy (MBE) systems in the late 1960s.[10–12]

This series of events emphasize the pivotal role played by MBE to precisely control the thickness and compositions of the semiconductor layers that comprise the resonant tunneling heterostructure. It should be noted that the first experiments concerning the growth of GaAs and AlGaAs layers by MBE were performed in 1968.[10,11] Six years later, high quality resonant tunneling structures were demonstrated at IBM.[13] However, it was only in 1985 that GaAs/AlGaAs resonant tunneling diodes (RTDs) were sufficiently optimized to operate at room temperature.[14,15] This milestone caught the attention of multiple research groups that started working on this topic, both from a fundamental angle, to understand the physics of resonant tunneling transport, and also from a practical perspective, to engineer ultrafast electronic and photonic devices.[16]

In contrast to the 17 years elapsed between the initial MBE growth of nonpolar III–V semiconductors[10,11] and the successful engineering of room-temperature RTDs,[14,15] in polar III-nitride semiconductors, the development of GaN/AlN RTDs was remarkably different. The first report about the MBE growth of nitride semiconductors was published in 1975.[17] However, we should point out that Isamu Akasaki had already grown GaN by MBE in 1973.[18] Despite these early pioneering results, it would take 43 years—until 2016—to demonstrate the first III-nitride resonant tunneling diode that exhibits repeatable negative differential conductance (NDC) at room temperature.[19]

In this paper, we present, from the epitaxial growth perspective, an account of how we solved the problem of engineering resonant tunneling transport in III-nitride heterostructures. By combining detailed polar-heterostructure design, precise epitaxial growth, and advanced fabrication techniques, we have demonstrated robust resonant tunneling transport in multiple III-nitride RTD designs. The repeatable and robust resonant transport in our devices allowed us to uncover the fundamental physics of resonant tunneling injection in polar heterostructures[19–22] and demonstrate the first practical application: the III-nitride resonant tunneling oscillator.[23]

In Secs. II–IV, we discuss the multiple aspects of GaN/AlN RTD growth by MBE and their correlation with electronic transport at room temperature. We start by introducing the use of RHEED to monitor—in real time—the number of atomic monolayers incorporated into the crystal. This technique allows us to deterministically control the number of monolayers in the tunneling barriers and experimentally measure the exponential relationship between barrier thickness and magnitude of the resonant tunneling current. In addition, we also study the effect of substrate temperature on the repeatable NDC of multiple RTDs grown at increasingly high temperatures. After optimizing these MBE growth conditions, we experimentally determine the implications of using substrates with different dislocation densities for the epitaxy of the GaN/AlN double-barrier heterostructures. Toward this goal, we fabricate and measure multiple RTDs with varying mesa areas and compare their room-temperature transport characteristics. These new insights into the MBE growth of nitride-based resonant tunneling devices represent a significant step forward in the engineering of new functionalities within the family of III-nitride semiconductors, providing a route to harness quantum interference effects for the new generation of electronic and photonic devices.

II. EPITAXIAL GROWTH OF GaN/AlN DOUBLE-BARRIER HETEROSTRUCTURES

Resonant tunneling devices rely on the engineering of a resonant cavity in which constructive quantum interference effects lead to an exponential increase in the amplitude of the electronic wave function. The resonant cavity is usually formed by a thin quantum well flanked by two tunneling barriers. In these structures, attaining atomically smooth interfaces is of paramount importance in order to preserve electronic coherence, thereby enabling constructive quantum interference. This requirement was identified right after the first demonstration of NDC in GaAs/AlGaAs double-barrier heterostructures.[14] These pioneering studies revealed that the growth of sharp heterointerfaces, on the order of the electron wavefunction, are crucial for the realization of high performance double-barrier resonant tunneling structures.

The epitaxial growth of smooth III-nitride films is achieved under metal-rich growth conditions. Within this regime, the adatom diffusivity at the growth front is favored by the presence of a metallic adlayer, which reduces the diffusion barrier height.[24,25] To obtain atomically smooth interfaces, the step-flow growth mode within the intermediate regime should be maintained throughout the whole epitaxial process. To verify the presence of this metallic adlayer, we track the intensity of the RHEED.[26] Figure 1(a) shows the typical RHEED pattern projected on a fluorescent screen and captured by an external camera during the MBE growth of a GaN/AlN RTD. Our devices are grown along the [0001]-direction of single-crystal n-type GaN substrates. Unless otherwise specified, the wafers exhibit a typical threading dislocation density (TDD) $\approx 5 \times 10^4\ \mathrm{cm}^{-2}$ and a nominal offcut angle of $\approx 0.3^\circ$ toward the m-axis. The device structure comprises two n-type GaN contacts, each with a thickness of 100 nm and degenerately doped with silicon donors. The active region includes an unintentionally doped (UID) GaN spacer of 10 nm, two 2-nm thick AlN tunneling barriers on each side of a 3-nm wide GaN quantum well, and a collector spacer 3-nm thick, as shown in Fig. 1(b). The asymmetric spacers and doping levels were chosen to limit the extension of the collector depletion region, thereby reducing the electric field inside the GaN quantum well, resulting in a lower resonant tunneling voltage.[27]

In conjunction with metal-rich growth conditions, another critical aspect of the MBE growth of RTDs is attaining precise control over the thickness of the AlN tunneling barriers. In this regard, it is important to note that aluminum desorption is strongly suppressed at typical GaN growth temperatures (i.e., $700\,^\circ\mathrm{C} < T_S < 800\,^\circ\mathrm{C}$). The lack of desorption kinetics during the AlN growth implies that all the adsorbed aluminum atoms eventually incorporate into the crystal. Therefore, it becomes imperative to precisely control the amount of Al atoms deposited on the substrate. To overcome this issue, we continuously track the intensity of the RHEED pattern,[28–32] allowing us to monitor, in real time, the incorporation of single atomic monolayers (MLs) in each of the tunneling barriers.[33] In Fig. 1(f), we show the intensity of the RHEED pattern recorded during the growth of the AlN/GaN/AlN

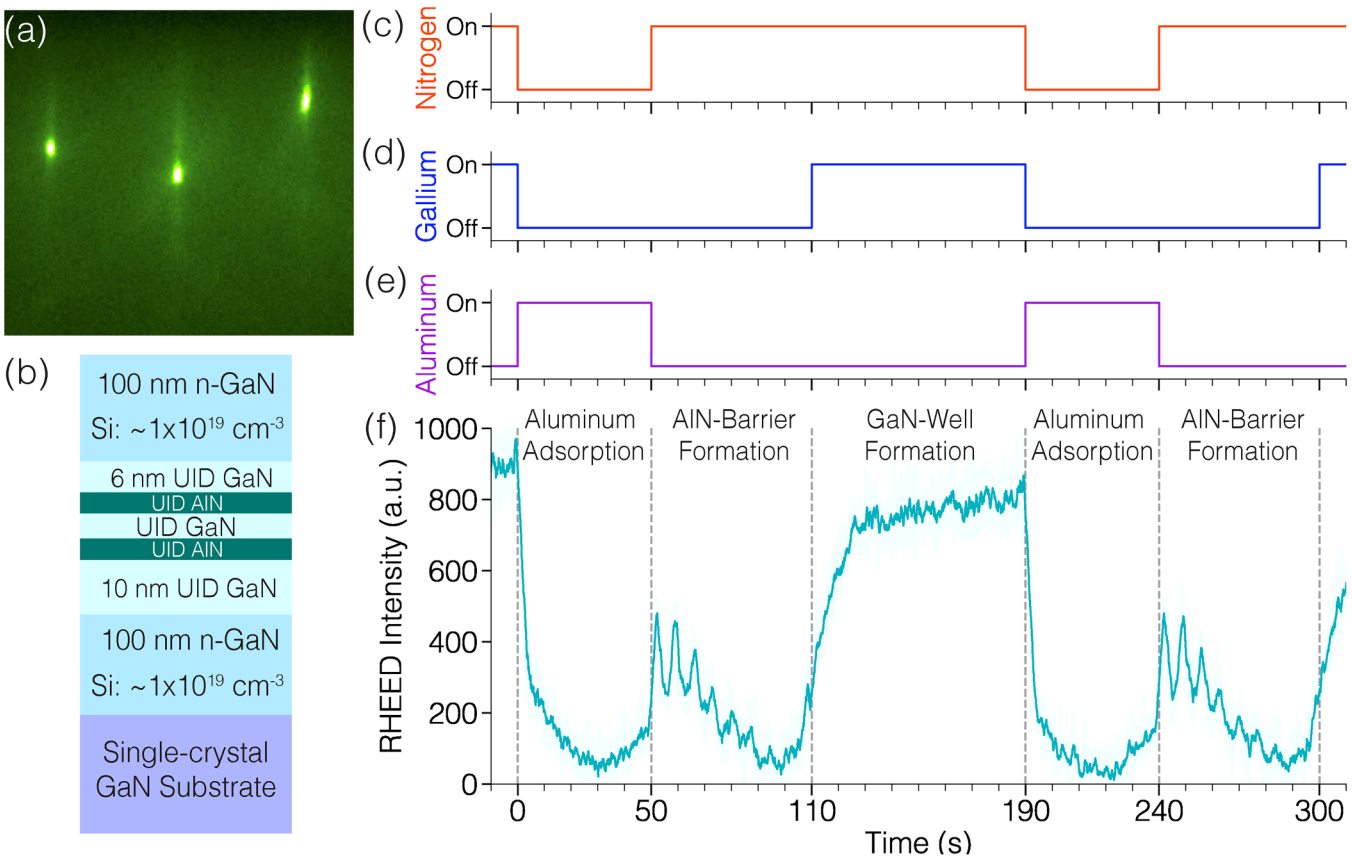

FIG. 1. Molecular beam epitaxy is employed to grow GaN/AlN RTDs. (a) During growth, RHEED is employed to monitor the growth front, verifying the presence of a metallic adlayer. (b) The RTD device structure comprises two n-type GaN contacts which sandwich the AlN/GaN/AlN active region. Panels (c)–(e) show the shutter status vs time for the nitrogen plasma source, gallium, and aluminum effusion cells. (f) The intensity of the RHEED pattern is continuously monitored during the growth of the AlN/GaN/AlN active region. The AlN barriers are grown using a two-step procedure, which consists of (1) aluminum adsorption and (2) AlN-barrier formation. In each of these steps, only aluminum and then only nitrogen shutters are open. Following the formation of the emitter barrier, the GaN quantum well is grown providing, at the same time, both nitrogen and gallium atoms. Finally, the collector tunneling barrier is also grown using the two-step procedure described previously.

double-barrier active region, maintaining a constant substrate temperature, $T_s = 775\,^{\circ}\mathrm{C}$. Initially, we deposit Al atoms by opening the shutter of the aluminum effusion cell during 50 s, as shown in the on/off plot of the aluminum shutter [see Fig. 1(e)]. Immediately after the deposition of aluminum atoms, the Al-shutter is closed and the N-shutter is opened, resulting in the incorporation of the first AlN tunneling barrier. From the number of oscillations in the RHEED intensity, shown in Fig. 1(f), we can ascertain that seven atomic monolayers of AlN are incorporated into the crystal, forming the emitter tunneling barrier. Furthermore, by timing each of these oscillations, we can also determine the growth rate of ~7 s/ML, employing a plasma power of 200 W and a nitrogen flow rate of 1.0 SCCM. We highlight that using this growth technique, it is possible to precisely control the amount of aluminum required for the formation of an AlN barrier with a thickness corresponding to an integer number of AlN monolayers.[33] As shown in Fig. 1(f), the amount of aluminum is controlled by the effusion cell temperature and the deposition time.[34] Thus, the uncoupling between the growth rate and the aluminum adsorption time allows us to prevent the formation of Al droplets after the growth of the AlN barriers, which is key for achieving atomically sharp interfaces.

Both the top and bottom n-type GaN contact layers, as well as the UID-GaN quantum well, are grown under similar metal-rich growth conditions, with a substrate temperature of $T_s = 775$. Nitrogen is supplied to the rf plasma source at a constant flow rate of 1.0 SCCM. The source power is set at 200 W, while the metal to nitrogen flux ratio is determined to be $\phi_{Ga}/\phi_N \approx 1.2$. As can be seen from Figs. 1(c), 1(d), and 1(f), both the nitrogen and gallium shutters are opened during the formation of the quantum well, resulting in the continuous growth of GaN. After the well is formed, we repeat the two-step procedure described previously to incorporate the AlN barrier on the collector side. It is important to highlight that the excess Ga does not incorporate into the crystal because the N-shutter is closed during the aluminum adsorption

step. This can be seen in Fig. 1(f); between the time marks of 190 s and 240s we keep only the aluminum shutter open. Therefore, excess gallium from the previous step desorbs from the surface that is being covered by aluminum atoms at the same time. This growth procedure enables the formation of atomically sharp interfaces since no excess aluminum nor excess gallium is present during the interface formation on each side of the GaN quantum well.

After the epitaxial growth, the resonant tunneling heterotructures are inspected using optical microscopy to determine the presence of gallium droplets, thus confirming metal-rich growth conditions throughout the whole epitaxial process. Atomic force microscopy (AFM) is also employed to scan the top surface of the device structure. AFM scans over different areas, $2 \times 2\,\mu m^2$ and $20 \times 20\,\mu m^2$, reveal a smooth surface morphology, showing the presence of terraces and atomic steps, indicative of the step-flow growth mode. In addition, x-ray diffraction (XRD) is also employed to measure the thicknesses of the barriers and width of the quantum well by fitting the intensity of the diffracted x rays with a theoretical model.

A. Effect of substrate growth temperature on resonant tunneling transport characteristics

Whereas the step-flow growth mode under metal-rich conditions can be readily obtained for the GaN growth between 700 and 800 °C,[35] attaining the same growth mode for AlN films requires higher temperatures.[36] This mismatch in growth parameters results in higher sticking coefficients and shorter diffusion lengths for Al adatoms. The high sticking coefficient implies that all the adsorbed aluminum incorporates into the crystal as the growth proceeds. Therefore, it is important to precisely control the amount of aluminum deposited, which determines the thickness of the AlN tunneling barriers. As discussed in Sec. II, using the two-step modulation of aluminum and nitrogen fluxes, we can deposit a total amount of Al closely commensurate with an integer number of atomic monolayers of the AlN crystal. Following the deposition of aluminum, the excess metal present on the surface helps reduce the diffusion barrier experienced by the aluminum atoms, allowing them to find the most stable atomic sites within the growth front. This process is strongly influenced by the substrate temperature that controls the diffusion length of the adatoms. Therefore, in this section, we experimentally investigate the important effects of substrate temperature on the resonant tunneling transport characteristics of GaN/AlN double-barrier heterostructures.

To uncover the effects of substrate growth temperature on the quantum transport characteristics of nitride RTDs, we prepared three different devices grown at increasingly high temperatures. Table I presents the main results for three RTD samples grown at $T_S = 700\,^{\circ}C$, $740\,^{\circ}C$, and $775\,^{\circ}C$. It is important to point out that these temperatures are kept constant throughout the whole epitaxial process. Atomic force microscopy reveals that each of these samples presents a smooth surface morphology with clear atomic steps and subnanometer root-mean-square (rms) roughness. The AFM scans over an area of $2 \times 2\,\mu m^2$ are shown in the second row of Table I. A gradual improvement in the rms roughness has been observed as the temperature increases. At 700 °C, we can see a surface morphology characterized by the formation of step bunches, resulting in a rms roughness of 0.326 nm. In contrast, the samples grown at higher temperatures do not exhibit step bunching, however, a zigzag shape of the atomic steps is clearly visible. This step morphology is characteristic of nitride films grown on substrates with miscut orientation toward the $[11\bar{2}0]$-direction, along the m-axis.[37,38]

Following the structural characterization, we fabricate the samples into RTDs using conventional contact lithography, reactive ion etching (RIE), and electron beam evaporation. Diodes with areas between 6 and $400\,\mu m^2$ are fabricated employing a self-aligned process. Fabrication starts with the deposition of the collector metal contact formed by the stack of metal layers in the following order: Ti/Au/Ni, with thickness 20/180/50 nm, respectively. After lift-off, the collector contact is used as etching mask, defining multiple RTD mesa areas. Dry etching is carried out using a gas mixture of Ar, Cl_2, and BCl_3, which is ignited to produce a plasma with an etch rate of ∼100 nm/min. Finally, the emitter metal contact, formed by Ti/Au metal layers, is also evaporated and patterned by lift-off, resulting in the device structure shown schematically in the inset of Fig. 2(c).

After fabrication, each of the samples is tested at room temperature employing a semiconductor parameter analyzer. The current-voltage (J-V) characteristics of each structure are measured under forward and reverse bias conditions using double-sweep scans, with injection currents up to $15\,kA/cm^2$. When the diodes are biased in the forward direction, a region of NDC is measured in each sample. To verify the repeatable nature of the resonant tunneling peak and NDC, multiple double-sweep scans are successively recorded. The fourth row of Table I presents the measured J-V characteristics of a representative device fabricated in each of these heterostructures grown at different substrate temperatures.

In the case of the RTD structure grown at $T_S = 700\,^{\circ}C$, we observe that the current peak exhibits a voltage shift during the first double-sweep scan. The arrows within this plot indicate the direction of the voltage bias sweep. During the first upward sweep, the resonant tunneling peak is measured at ∼10.7 V with an injection current of $\sim 5.7\,kA/cm^2$ and a peak-to-valley current ratio (PVCR) of ∼1.5. In contrast, during the downward sweep of the same scan, we observe that the peak voltage increases to ∼12.9 V and the PVCR decreases to ∼1.3. This shift in the peak voltage and reduction of the PVCR, suggests the presence of traps which modify the electrostatics of the double-barrier structure. However, despite the presence of these crystal imperfections, resonant tunneling injection is the dominant transport mechanism in these devices. This is confirmed by the measurement of clear room-temperature NDC under both upward and downward voltage bias sweeps. Furthermore, during the subsequent closed-loop bias scans, we observe that the peak voltage eventually stabilizes at ∼13.2 V with a repeatable peak current density of $\sim 6.4\,kA/cm^2$. Thus, despite the presence of defects within the active region, they do not prevent resonant tunneling transport and NDC at room temperature.[20]

Table I also displays the J-V characteristics of the RTD structures grown at higher temperatures: $T_S = 740\,^{\circ}C$ and $T_S = 775\,^{\circ}C$. For both of these samples, we can see that the peak and valley voltages exhibit a repeatable value for every single double-sweep bias scan. This important difference compared to

TABLE I. Effect of substrate temperature during the MBE growth. A series of GaN/AlN double-barrier RTDs are grown at different substrate temperatures to experimentally determine its effect on electronic transport. After growth, we measure the morphology of the top surface using atomic force microscopy (AFM) and determine the root-mean-square roughness. X-ray diffraction, not shown here, is also performed to confirm the designed layer structure of each sample. After growth, the heterostructures are fabricated into diodes and their electronic transport characteristics are measured at room temperature. To determine the repeatable behavior of the resonant tunneling peak and negative differential conductance, multiple double-sweep scans are measured. We present the current-voltage (J-V) characteristics of a representative device fabricated in each sample. The effect of substrate temperature on the device yield is also shown in the bottom row.

Growth Temp.	700 °C	740 °C	775 °C
AFM Scan	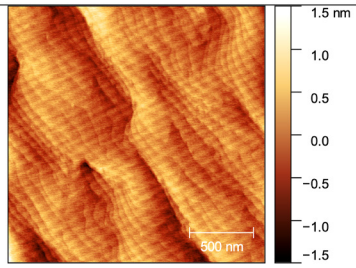	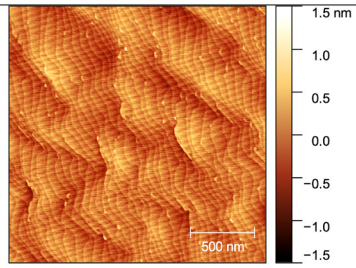	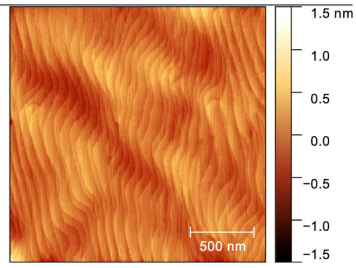
Surface roughness	0.326 nm	0.216 nm	0.146 nm
Room Temp. Current-Voltage	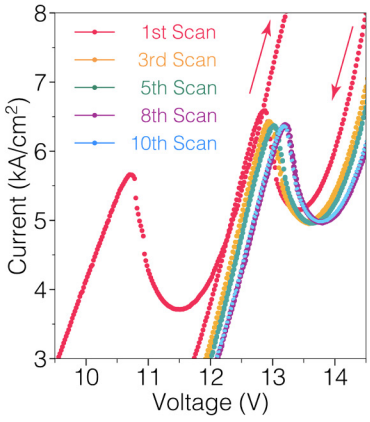	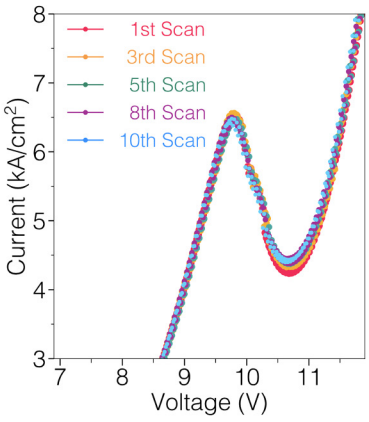	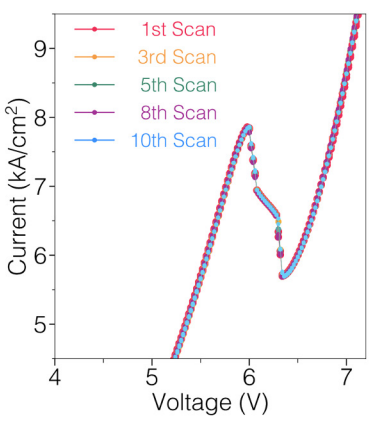
Device Yield	12 %	55 %	91 %

diodes grown at $T_S = 700\,^{\circ}\mathrm{C}$ indicates that the use of higher substrate temperature prevents the formation of charge traps within the resonant structure. Moreover, from the J-V characteristics of the RTD grown at $T_S = 740\,^{\circ}\mathrm{C}$, it is clear that the valley current exhibits a small increment between the first and the eighth scans. This small increment in the valley current leads to a slight decrease in the PVCR, which is measured at ∼1.52, during the first scan, and then it reduces to ∼1.43, during the tenth and subsequent scans. In contrast, for the diode grown at $T_S = 775\,^{\circ}\mathrm{C}$, the valley current exhibits a constant magnitude which remains unchanged during the multiple voltage scans. As a consequence, the PVCR exhibits a constant value of ∼1.40 for every single scan at room temperature. To get further insight into the scattering processes that determine these experimentally measured PVCRs, we employ our analytical quantum transport model for polar RTDs.[22] Using this framework, we calculate the current-voltage characteristics of our resonant heterostructures under different electronic transport regimes, from completely coherent resonant injection to the limit of sequential tunneling transport. Our calculations indicate that, at room temperature, a PVCR of ∼3.5 is expected for the RTD structure with 2-nm AlN barriers and a 3-nm wide GaN quantum well. It is important to highlight that in our model, we have assumed that the main dephasing mechanism that limits coherent resonant tunneling injection is electron-phonon scattering. However, nitride RTDs with this high PVCR have not been reported so far in the literature. One potential reason for this discrepancy could be due to the presence of considerable interface roughness scattering that might get exacerbated by the strong internal electric fields across the double-barrier active region.

In closing this section, we set out to conclusively verify the improvement in the tunneling transport characteristics for the diodes grown at substrate temperatures close to $T_S = 775\,^{\circ}\mathrm{C}$. Toward this goal, we perform device yield analysis in each of the samples presented in Table I. A total of 150 devices featuring different mesa

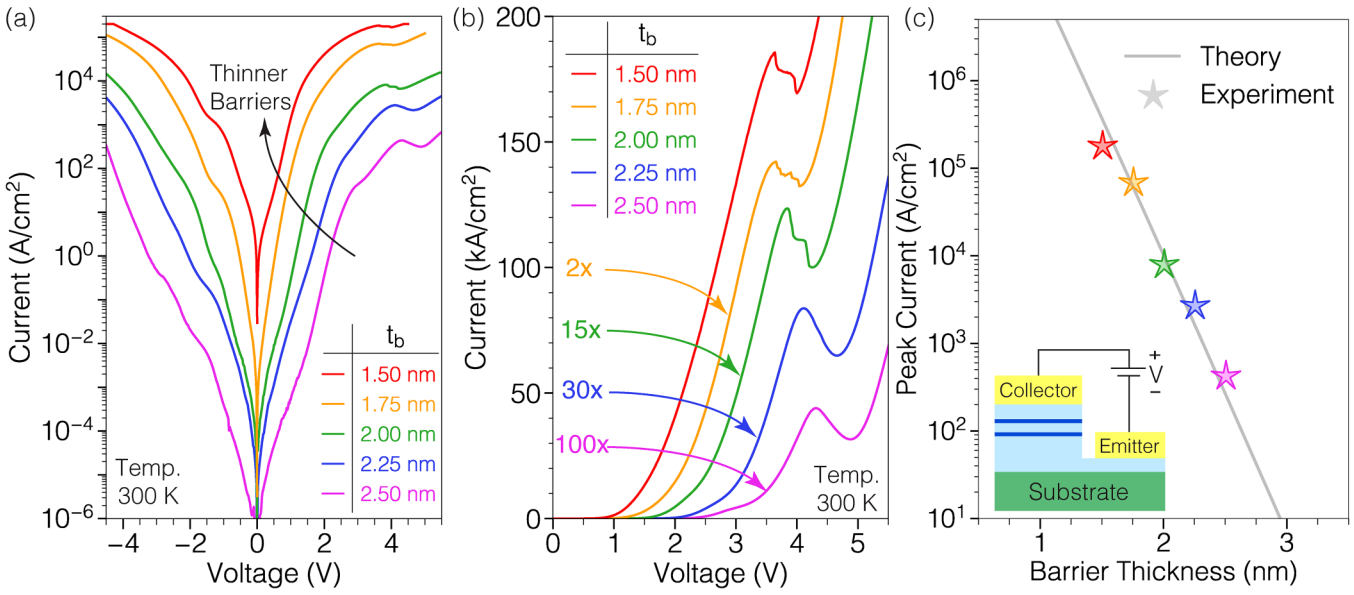

FIG. 2. Different magnitudes of resonant tunneling current are engineered in GaN/AlN double-barrier heterostructures by systematically varying the thickness of the AlN barriers. Using RHEED intensity oscillations we control the number of AlN monolayers incorporated into the tunneling barriers. Using this method, we grow five different RTD samples with fixed quantum well width $t_w = 3$ nm and variable AlN-barrier thickness $t_b = 1.5$, 1.75, 2.0, 2.25, and 2.5 nm. (a) Room-temperature current-voltage (J-V) characteristics are measured from each of these double-barrier structures, under both bias polarities. The semilogarithimc plot shows the exponential control of barrier thickness over the magnitude of the resonant tunneling current. (b) Under forward bias, the characteristic resonant tunneling peak and negative differential conductance are measured in each of our devices at room temperature. Because of the exponential relationship between barrier thickness and electronic transmission, the magnitude of the peak current is modulated over three orders of magnitude when the barrier thickness decreases from 2.5 nm down to 1.5 nm. The measured tunneling currents in (b) are scaled by different factors to facilitate direct comparison. (c) The experimental peak tunneling currents agree well with the values predicted by our analytical RTD transport model. [20]

areas between 4 and 400 μm^2 were measured across each of the $1 \times 1\ cm^2$ RTD samples. From this set of measurements, we calculate the experimental device yield given by the percentage of devices that exhibit repeatable NDC at room temperature. Table I shows a clear correlation between device yield and substrate temperature. Whereas a low yield of 12% is obtained for the RTD sample grown at $T_S = 700\,^{\circ}C$, this metric increases to 91% for the double-barrier structure grown at $T_S = 775\,^{\circ}C$. This trend indicates that higher substrate temperatures prevent the formation of trapping defects within the double-barrier active region, thereby preserving electronic coherence and allowing the measurement of robust room-temperature resonant tunneling transport in GaN/AlN RTDs.

B. Control of the barrier thickness by RHEED intensity oscillations

The possibility of engineering ultrafast carrier transport dynamics across double-barrier heterostructures makes RTDs attractive for the manufacture of compact, high-power electronic oscillators. In these devices, the gain provided by the resonant heterostructure is harnessed to drive an oscillator circuit and generate RF signals with cutoff frequencies inside the terahertz band.[39] RTD oscillators based on well established semiconductor materials such as GaAs/AlAs[40] and InGaAs/AlAs[41] have been reported over the last decades. In contrast, III-nitride RTD oscillators have not been studied in detail yet. In fact, recently, we have reported the first microwave electronic oscillators driven by GaN/AlN RTDs grown along the Ga-polar[23] as well as the N-polar[42] directions of the wurtzite lattice. This important milestone attests to the high degree of electronic coherence across the nitride resonant tunneling cavity, thereby raising hopes for the demonstration of RF power generation within the mm-wave and terahertz bands.[43–45] Toward this goal, higher current levels as well as optimal management of the parasitic elements would be required to push the cutoff frequencies well inside the terahertz band. Consequently, this is an area in which further improvement is expected during the following years to optimize nitride resonant tunneling cavity for high-power and high-frequency applications.

In this section, we show that by using *in situ* RHEED intensity oscillations, we can accurately determine the number of monolayers that form the AlN barriers and thus control the magnitude of the resonant tunneling current in our devices. Employing this method, we prepare five different RTD structures with fixed quantum well width $t_w = 3$ nm and variable barrier thickness $t_b = 1.5$, 1.75, 2.0, 2.25, 2.5 nm. Due to the exponential relationship between the AlN barrier thickness and amplitude of the electronic transmission, the magnitude of the tunneling current is exponentially enhanced over several orders of magnitude. This behavior has been experimentally measured in our devices and can

be seen in Fig. 2(a), which shows the room-temperature J-V characteristics for each RTD, measured under both bias polarities. The main resonant tunneling peak as well as a region of NDC is measured in each device under forward current injection, as can be seen in Fig. 2(b). To facilitate direct comparison, in Fig. 2(b), we scale the forward-bias current of each device by a factor indicated by the arrows. The peak current density, measured from these devices, is exponentially enhanced from ~440 up to ~186 kA/cm^2 by varying the thicknesses of the tunneling barriers from 2.5 nm down to 1.5 nm.

III-nitride RTDs exhibit strong internal polarization fields that dictate not only the magnitude of the resonant tunneling voltage but also the electronic transmission probability across the polar double-barrier heterostructure.[22] The control exerted by the intense polarization fields has been elucidated a few years ago employing a combined experimental and theoretical approach.[20] To quantitatively determine the scaling of the peak tunneling current as a function of the barrier thickness, we employ the analytical RTD model introduced in Ref. 20. Figure 2(c) shows the good agreement between the experimentally measured peak current densities, extracted from the J-V curves in Fig. 2, and the theoretical peak current density obtained from our analytical RTD model. These results indicate that further scaling of the AlN barriers is necessary to obtain current densities on the order of $\sim 1 \times 10^6$ A/cm^2, as required by ultra-high speed RF applications.

III. GaN/AlN RTDs GROWN ON SUBSTRATES WITH DIFFERENT DISLOCATION DENSITIES

Repeatable room-temperature NDC in III-nitride RTDs has been recently demonstrated not only in devices grown on single-crystal GaN substrates[20,46,47] but also on GaN template films grown atop sapphire substrates.[48,49] However, due to the larger density of dislocations and defects derived from the heteroepitaxial growth, the device yield within this platform is limited to approximately 45%, for RTDs with areas between 0.88 and 113 μm^2.[49] This metric contrasts with the device yield of 91% obtained for RTDs grown on the single-crystal GaN substrate and with mesa areas varying between 4 and 400 μm^2 (see Table I). This dramatic reduction in device yield explains the great difficulties in measuring resonant tunneling transport in the first III-nitride RTDs fabricated in the early 2000s.[50,51] The important effects on the device performance and yield derived from the presence of dislocations and substrate defects have been under study during the last decades. In particular, one of the long-standing questions to be answered is the great tolerance of many nitride-based devices such as blue LEDs to the presence of high densities of dislocations.[52]

Resonant tunneling transport, being extremely sensitive to crystal defects that degrade electronic coherence, could be employed to better understand the consequences of threading dislocations in the charge transport characteristics of vertical III-nitride devices. With this goal in mind, we have grown GaN/AlN double-barrier RTDs on single-crystal n-type GaN substrates with different TDDs. Both structures were grown under optimal growth conditions and using precise control over the thickness of the layers that comprise the double-barrier active region. We employed two different substrates with TDD$_1 \approx 5 \times 10^4$ cm^{-2} and TDD$_2 \approx 5 \times 10^6$ cm^{-2}, as specified by the commercial substrate suppliers. The nominal offcut angle of the epitaxial surface, quoted from the corresponding wafer datasheets are $\phi_1 \approx 0.35^\circ$ and $\phi_2 = 0.35 \pm 0.15^\circ$ toward the m-axis, respectively. After the MBE growth, the heterostructures are characterized using AFM and XRD, we then fabricate devices following the procedure detailed in Subsection II A. To uncover the influence of the dislocation density on the electronic tunneling transport, we fabricate devices with different mesa areas and measure their J-V characteristics at room temperature.

Figure 3 shows the J-V characteristics for multiple devices with different mesa areas, measured across both samples. As a first observation, we highlight that no appreciable difference in device yield was observed between the two samples. To evaluate the effects derived from the presence of threading dislocations in each sample, we perform electronic transport measurements on RTDs with different mesa areas between 8×8 and $18 \times 18\,\mu$m^2. Figures 3(a) and 3(b) show the J-V curves for the sample with TDD$_1 \approx 5 \times 10^4$ cm^{-2}. From Fig. 3(a), we can see that for current densities $J > 1 \times 10^{-1}$ A/cm^2, the measured current density is independent of the device area. However, for lower injection levels (i.e., $J < 1 \times 10^{-1}$ A/cm^2), the current density scales with the area of the device being measured. This observation reveals that despite the low dislocation density, conduction via threading dislocations might play a role within the low current injection regime. In contrast, as the bias voltage increases and the resonant tunneling current is exponentially enhanced, the contribution of these leakage paths becomes negligible compared to the dominant resonant tunneling transport injection. At room temperature, the peak current density is measured at $J_p = 10.5 \pm 0.75$ kA/cm^2, with a PVCR of ~1.36 for multiple devices with different mesa areas. Furthermore, from Fig. 3(b), we can see that the reverse bias threshold voltage, measured at ~ -3.5 V, is completely independent of the device area. This is expected since the threshold voltage is measured at a current level of $J \approx 1$ kA/cm^2 in which tunneling injection is the dominant transport mechanism.

The room-temperature J-V characteristics for the RTD structures with TDD$_2 \approx 5 \times 10^6$ cm^{-2} are plotted in Figs. 3(c) and 3(d). In contrast to the former RTD sample, we can see from Fig. 3(c) that the higher density of threading dislocations plays a bigger role as the device area increases. Particularly, under reverse bias conditions, it is evident that the current densities exhibit a monotonic increase with the area of the device being measured. These experimental results reveal that the presence of a higher density of dislocations dramatically affects device performance. However, it is important to highlight that the increase in leakage current does not prevent the measurement of repeatable room-temperature NDC in these devices. This can be seen from Fig. 3(d), which shows the linear plot of the same data presented in Fig. 3(c). We note, however, that as the device area scales up, the peak current density also increases and the PVCR exhibits a decreasing trend. For the devices with mesa areas of $8 \times 8 \Rightarrow 10 \times 10 \Rightarrow 14 \times 14 \Rightarrow 18 \times 18\,\mu$m^2, we measured a room-temperature PVCR of $1.29 \Rightarrow 1.24 \Rightarrow 1.14 \Rightarrow 1.11$. In contrast, the RTDs with lower TDD shown in Figs. 3(a) and 3(b) exhibit a higher PVCR of 1.36 at room temperature, which is independent of the device area. Under reverse bias conditions, we can see that the threshold voltage is strongly affected by the leakage current, which increases

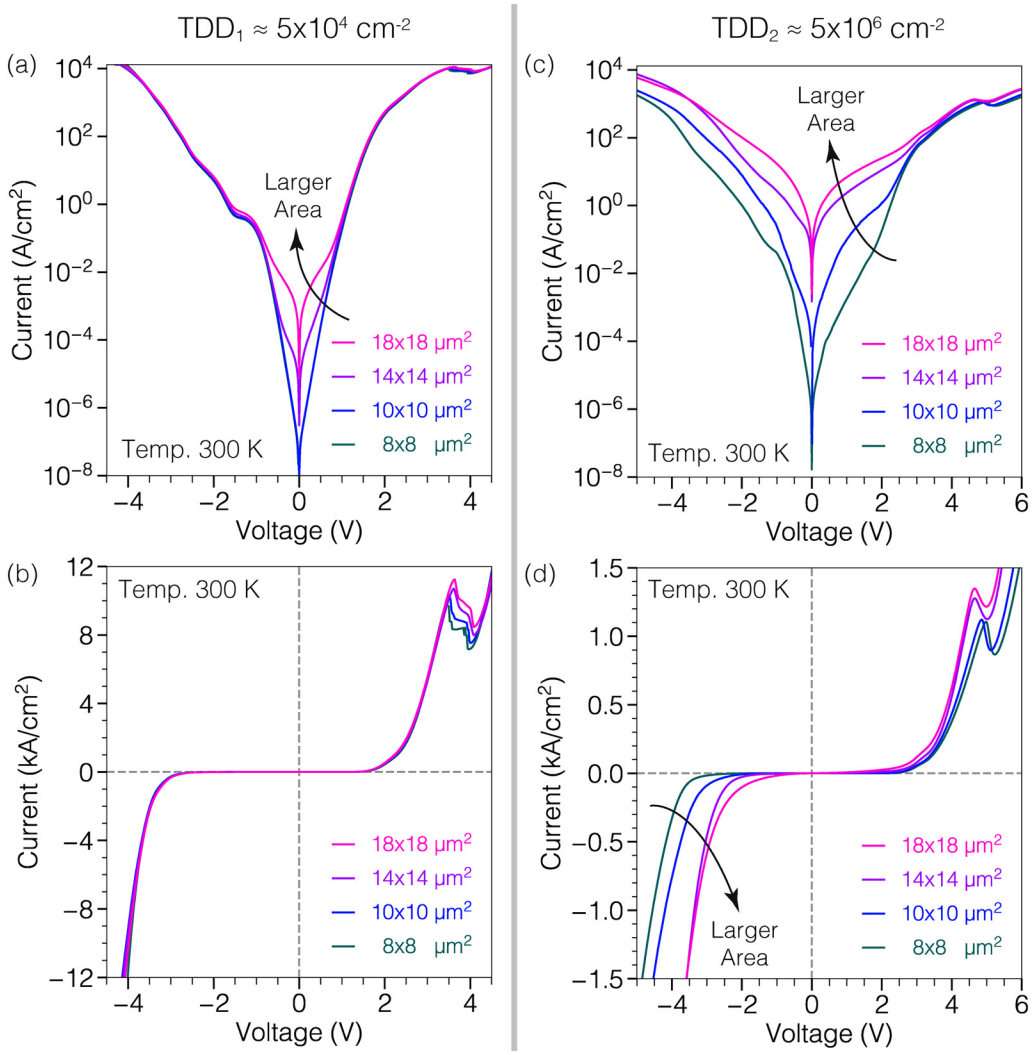

FIG. 3. GaN/AlN RTDs are grown and fabricated on single-crystal n-type GaN substrates with different TDDs. Both structures were grown under optimal growth conditions and using precise control over the thickness of the layers that comprise the double-barrier active region. (a) and (b) show the current-voltage characteristics of various RTDs with different mesa areas, fabricated in the sample with $TDD_1 \approx 5 \times 10^4$ cm^{-2}. (c) and (d) display the current-voltage characteristics of multiple RTDs, with different mesa areas, fabricated in the sample with $TDD_2 \approx 5 \times 10^6$ cm^{-2}.

with device area [see Fig. 3(d)]. These results reveal the high sensitivity of III-nitride resonant tunneling diodes to the presence of leakage paths due to threading dislocations. However, further studies will be required to obtain a greater understanding into the fundamental electronic transport mechanisms through threading dislocations and their impact on the performance of vertical electronic and photonic III-nitride devices.

IV. CONCLUDING REMARKS

In summary, we have presented a detailed account of the crucial developments in the epitaxial growth of III-nitride heterostructures that have led us to the demonstration of robust resonant tunneling transport and reliable room-temperature NDC in III-nitride heterostructures. We showed that *in situ* tracking of the crystal electron diffraction allows us to deterministically control the number of monolayers incorporated into the tunneling barriers of the double-barrier active region. Employing this growth technique, we fabricated various GaN/AlN RTD designs showing the exponential enhancement of the resonant tunneling current as a function of barrier thickness. In addition, we experimentally demonstrate that tunneling transport across III-nitride RTDs is sensitive to epitaxial parameters such as substrate growth temperature and threading dislocation density. This new insight into the MBE

growth of nitride-based resonant tunneling devices represents a significant step forward in the engineering new functionalities within the family of III-nitride semiconductors, allowing to harness quantum interference effects for the new generation of electronic and photonic devices.

ACKNOWLEDGMENTS

This work was supported, in part, by AFOSR (No. FA9550-20-1-0148), NSF RAISE TAQs (No. 1839196), the Semiconductor Research Corporation (SRC) Joint University Microelectronics Program (JUMP), NSF NewLaw (No. EFMA-1741694), and ONR (Nos. N00014-20-1-2176 and N00014-17-1-2414). This work made use of the shared facilities that are supported through Nos. NSF ECCS-1542081, NSF DMR-1719875, and NSF DMR-1631282.

DATA AVAILABILITY

The data that support the findings of this study are available from the corresponding author upon reasonable request.

REFERENCES

[1]L. De Broglie, Ann. Phys. **10**, 22 (1925).
[2]L. De Broglie, *Nobel Lectures on Physics 1922–1941* (Elsevier, Amsterdam, 1929), p. 244.
[3]J. R. Oppenheimer, Phys. Rev. **31**, 66 (1928).
[4]R. H. Fowler and L. Nordheim, Proc. R. Soc. Lond. A **119**, 173 (1928).
[5]G. Gamow, Z. Phys. **51**, 204 (1928).
[6]C. Zener, Proc. R. Soc. A **145**, 523 (1934).
[7]L. Esaki, Phys. Rev. **109**, 603 (1958).
[8]L. V. Iogansen, Sov. Phys. JEPT **18**, 146 (1964).
[9]L. V. Iogansen, Sov. Phys. JEPT **20**, 180 (1965).
[10]J. R. Arthur, J. Appl. Phys. **39**, 4032 (1968).
[11]J. E. Davey and T. Pankey, J. Appl. Phys. **39**, 1941 (1968).
[12]A. Y. Cho, J. Vac. Sci. Technol. **8**, S31 (1971).
[13]L. L. Chang, L. Esaki, and R. Tsu, Appl. Phys. Lett. **24**, 593 (1974).
[14]M. Tsuchiya, H. Sakaki, and J. Yoshino, Jpn. J. Appl. Phys. **24**, L466 (1985).
[15]T. J. Shewchuk, P. C. Chapin, P. D. Coleman, W. Kopp, R. Fischer, and H. Morkoç, Appl. Phys. Lett. **46**, 508 (1985).
[16]A. C. Gossard, W. Brown, C. L. Allyn, and W. Wiegmann, J. Vac. Sci. Technol. **20**, 694 (1982).
[17]S. Yoshida, S. Misawa, and A. Itoh, Appl. Phys. Lett. **26**, 462 (1975).
[18]I. Akasaki, Rev. Mod. Phys. **87**, 1119 (2015).
[19]J. Encomendero, F. Afroz Faria, S. M. Islam, V. Protasenko, S. Rouvimov, P. Fay, D. Jena, and H. G. Xing, "Repeatable room temperature negative differential conductance in GaN/AlN resonant tunneling diodes," Phys. Rev. X **7**, 041017 (2017).
[20]J. Encomendero, F. A. Faria, S. M. Islam, V. Protasenko, S. Rouvimov, B. Sensale-Rodriguez, P. Fay, D. Jena, and H. G. Xing, Phys. Rev. X **7**, 041017 (2017).
[21]H. G. Xing, J. Encomendero, and D. Jena, "New physics in GaN resonant tunneling diodes," Proc. SPIE **10918**, 109180Z (2019).
[22]J. Encomendero, V. Protasenko, B. Sensale-Rodriguez, P. Fay, F. Rana, D. Jena, and H. G. Xing, Phys. Rev. Appl. **11**, 034032 (2019).
[23]J. Encomendero, R. Yan, A. Verma, S. M. Islam, V. Protasenko, S. Rouvimov, P. Fay, D. Jena, and H. G. Xing, Appl. Phys. Lett. **112**, 103101 (2018).
[24]C. Adelmann, J. Brault, G. Mula, B. Daudin, L. Lymperakis, and J. Neugebauer, Phys. Rev. B **67**, 165419 (2003).
[25]J. Neugebauer, T. K. Zywietz, M. Scheffler, J. E. Northrup, H. Chen, and R. M. Feenstra, Phys. Rev. Lett. **90**, 056101 (2003).
[26]C. Adelmann, J. Brault, D. Jalabert, P. Gentile, H. Mariette, G. Mula, and B. Daudin, J. Appl. Phys. **91**, 9638 (2002).
[27]J. Encomendero, V. Protasenko, F. Rana, D. Jena, and H. G. Xing, Phys. Rev. Appl. **13**, 034048 (2020).
[28]C. E. C. Wood, Surf. Sci. **108**, L441 (1981).
[29]H. Sakaki, M. Tanaka, and J. Yoshino, Jpn. J. Appl. Phys. **24**, L417 (1985).
[30]Z. Yang, J. Vac. Sci. Technol. B **14**, 2354 (1996).
[31]B. Daudin and F. Widmann, J. Cryst. Growth **182**, 1 (1997).
[32]J. Massies and N. Grandjean, J. Cryst. Growth **201–202**, 382 (1999).
[33]J. Encomendero, D. Jena, and H. G. Xing, "Resonant tunneling transport in polar nitride heterostructures," in *High-Frequency GaN Electronic Devices* (Springer International, Cham, 2020), pp. 215–247.
[34]S. D. Burnham and W. Alan Doolittle, J. Vac. Sci. Technol. B **24**, 2100 (2006).
[35]G. Koblmüller, S. Fernández-Garrido, E. Calleja, and J. S. Speck, Appl. Phys. Lett. **91**, 161904 (2007).
[36]K. Lee, Y. Cho, L. J. Schowalter, M. Toita, H. G. Xing, and D. Jena, Appl. Phys. Lett. **116**, 262102 (2020).
[37]X. Q. Shen, K. Furuta, N. Nakamura, H. Matsuhata, M. Shimizu, and H. Okumura, J. Cryst. Growth **301–302**, 404 (2007).
[38]C. Skierbiszewski, Z. R. Wasilewski, I. Grzegory, and S. Porowski, J. Cryst. Growth **311**, 1632 (2009).
[39]M. Feiginov, J. Infrared Millimeter Terahertz Waves **40**, 365 (2019).
[40]E. R. Brown, T. C. L. G Sollner, C. D. Parker, W. D. Goodhue, and C. L. Chen, Appl. Phys. Lett. **55**, 1777 (1989).
[41]H. Kanaya, R. Sogabe, T. Maekawa, S. Suzuki, and M. Asada, J. Infrared Millimeter Terahertz Waves **35**, 425 (2014).
[42]Y. Cho, J. Encomendero, S.-T. Ho, H. G. Xing, and D. Jena, Appl. Phys. Lett. **117**, 143501 (2020).
[43]Y. Zhao *et al.*, Appl. Phys. Lett. **105**, 173508 (2014).
[44]H. O. C. Quispe, J. Encomendero, H. G. Xing, and B. S. Rodriguez, "Terahertz plasmon amplification in RTD-gated HEMTs with a grating-gate," in *Active Photonic Materials VIII*, International Society for Optics and Photonics Vol. 9920 (SPIE, Bellingham, WA, 2016), pp. 178–181.
[45]H. O. Condori Quispe, J. J. Encomendero-Risco, H. G. Xing, and B. Sensale-Rodriguez, Appl. Phys. Lett. **109**, 063111 (2016).
[46]D. Li, L. Tang, C. Edmunds, J. Shao, G. Gardner, M. J. Manfra, and O. Malis, Appl. Phys. Lett. **100**, 252105 (2012).
[47]T. A. Growden, D. F. Storm, W. Zhang, E. R. Brown, D. J. Meyer, P. Fakhimi, and P. R. Berger, Appl. Phys. Lett. **109**, 083504 (2016).
[48]D. F. Storm *et al.*, J. Vac. Sci. Technol. B **38**, 032214 (2020).
[49]D. Wang *et al.*, Adv. Electron. Mater. **5**, 1800651 (2019).
[50]A. Kikuchi, R. Bannai, K. Kishino, C.-M. Lee, and J.-I. Chyi, Appl. Phys. Lett. **81**, 1729 (2002).
[51]C. T. Foxon *et al.*, Phys. Status Solidi C **2392**, 2389 (2003).
[52]S. D. Lester, F. A. Ponce, M. G. Craford, and D. A. Steigerwald, Appl. Phys. Lett. **66**, 1249 (1995).